nature photonics

ARTICLES

https://doi.org/10.1038/s41566-021-00901-z

Check for updates

Quantum optics of soliton microcombs

Melissa A. Guidry[1,3], Daniil M. Lukin[1,3], Ki Youl Yang[1,3], Rahul Trivedi[1,2] and Jelena Vučković[1]✉

Soliton microcombs—phase-locked microcavity frequency combs—have become the foundation of several classical technologies in integrated photonics, including spectroscopy, LiDAR and optical computing. Despite the predicted multimode entanglement across the comb, experimental study of the quantum optics of the soliton microcomb has been elusive. In this work we use second-order photon correlations to study the underlying quantum processes of soliton microcombs in an integrated silicon carbide microresonator. We show that a stable temporal lattice of solitons can isolate a multimode below-threshold Gaussian state from any admixture of coherent light, and predict that all-to-all entanglement can be realized for the state. Our work opens a pathway toward a soliton-based multimode quantum resource.

Kerr optical frequency combs[1–3] are multimode states of light generated via a third-order optical nonlinearity in an optical resonator. When a Kerr resonator is pumped weakly, spontaneous parametric processes populate resonator modes in pairs. In this regime, Kerr combs can be a quantum resource for the generation of heralded single photons and energy-time entangled pairs[4–6], multiphoton entangled states[7–9] and squeezed vacuum[10–12]. When pumped more strongly, the parametric gain can exceed the resonator loss and give rise to optical parametric oscillation (OPO) and bright comb formation. The modes of a Kerr comb can become phase-locked to form a stable, low-noise dissipative Kerr soliton (DKS). This regime of Kerr comb operation has become the foundation of multiple technologies, including comb-based spectroscopy[13], LIDAR[14], optical frequency synthesizers[15] and optical processors[16].

Although the soliton microcomb has been mostly studied classically, it is nonetheless fundamentally governed by the dynamics of quantized parametric processes: each resonator mode is coupled to every other mode through a four-photon interaction. The multimode coupled processes of the DKS resemble those of the well-studied synchronously pumped OPO[17,18]. If the quantum processes can be harnessed, soliton microcombs may open a pathway toward the experimental realization of a multimode quantum resource[18–20] in a scalable, chip-integrated platform[21,22]. Recent demonstrations of a fully integrated squeezing measurement[23] and a squeezed below-threshold microcomb[24] provide a technological road map for developing the DKS state as a resource for continuous-variable quantum computing[25–28]; however, the quantum-optical properties of soliton microcombs have not yet been directly observed: the first glimpse into non-classicality was the recent measurement of the quantum-limited timing jitter of the DKS state[29,30].

Linearization[31]—the formal separation of the optical state into the mean field solution and the quantum fluctuations—is one approach to simplify the otherwise intractable many-body quartic Hamiltonian of the DKS. The result of this approximation is a quadratic Hamiltonian, where the classical amplitudes A_m, obtained, for example, through the spatiotemporal Lugiato–Lefever equation (LLE)[32], drive the spontaneous parametric processes between quantum modes $\hat{a}_j$:

$$\hat{H}_{\mathrm{int}} = -\frac{g_0}{2}\sum_{m,n,j,k}\delta_{\mathrm{FWM}}\left(A_m A_n \hat{a}_j^{\dagger}\hat{a}_k^{\dagger} + A_k^{*}A_n\hat{a}_j^{\dagger}\hat{a}_m + \mathrm{h.c.}\right) \quad (1)$$

where $\delta_{\mathrm{FWM}} = \delta_{(j+k-m-n)}$ is the four-wave mixing (FWM) mode number matching condition, g_0 is the nonlinear coupling coefficient, and h.c. is the Hermitian conjugate. This approximation has been used to model[33] the quantum correlations developed by a coherent soliton pulse after propagating through a fibre[34]. Unlike the fibre soliton, however, the microcavity soliton features an interplay of dissipation and strong Kerr interactions in the regime where linearization can break down and yield unphysical predictions[35,36]. Experimentally verifying the validity of this model for the DKS is a prerequisite for exploring its application in quantum technologies.

In this work we use second-order photon correlation measurements to experimentally validate the linearized model (equation (1)) for describing the spontaneous parametric processes in DKS states. We first study the quantum formation dynamics of Kerr frequency combs, including coherence broadening of spontaneous FWM photon pairs near the OPO threshold. We then identify a class of DKS states—perfect soliton crystals[37,38]—which naturally isolate a subset of quantum optical fields from the coherent mean-field (Fig. 1); we measure the correlation matrix of the below-threshold modes to numerically infer the multimode entanglement structure of the state. We find that the DKS state may be engineered as an on-chip source of all-to-all entanglement.

The observation of the full optical spectrum of a Kerr frequency comb—including the above- and below-threshold processes—requires single-photon sensitivity and a high dynamic range. For this purpose, we designed a single-photon optical spectrum analyser (SPOSA) using multipass grating monochromators and superconducting nanowire single-photon detectors (SNSPDs; PhotonSpot). The SPOSA has a broadband (>200 nm) quantum efficiency of around 20%, and close-in dynamic range of >140 dB at ±0.8 nm. We generate Kerr frequency combs using microring resonators with a 350 GHz free spectral range (FSR) fabricated in 4H-silicon carbide-on-insulator, a platform with favourable nonlinear[39] and quantum[40] optical properties. With intrinsic quality factors (Q) as high as 5.6×10^6, low-threshold OPO (0.5 mW) and low-power soliton operation (2.3 mW) are achieved (Supplementary Fig. 4). We use the SPOSA to characterize the Kerr microcomb spectra through all stages of DKS formation (Fig. 2a,b). The sech^2 soliton envelope is seen to persist at the tails of the DKS, in modes with very low photon number $\left\langle a_j^{\dagger}a_j\right\rangle < 10^{-3}$ (corresponding to a photon count rate of <1 kHz). The quantum fluctuations generated in the DKS

[1]E. L. Ginzton Laboratory, Stanford University, Stanford, CA, USA. [2]Max-Planck-Institute for Quantum Optics, Garching, Germany. [3]These authors contributed equally: Melissa A. Guidry, Daniil M. Lukin and Ki Youl Yang. ✉e-mail: jela@stanford.edu

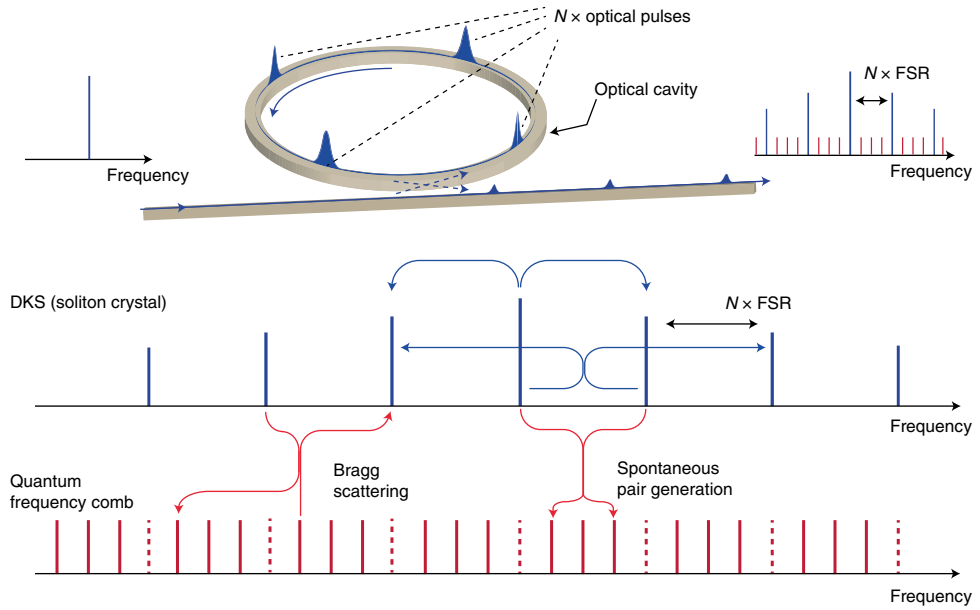

Fig. 1 | Linearized model for quantum optical fields in a DKS state. A schematic depiction of a Kerr microresonator with a circulating perfect soliton crystal state. The full optical state is modelled as a coherent classical comb (blue) that drives the quantum comb (red) via spontaneous parametric processes.

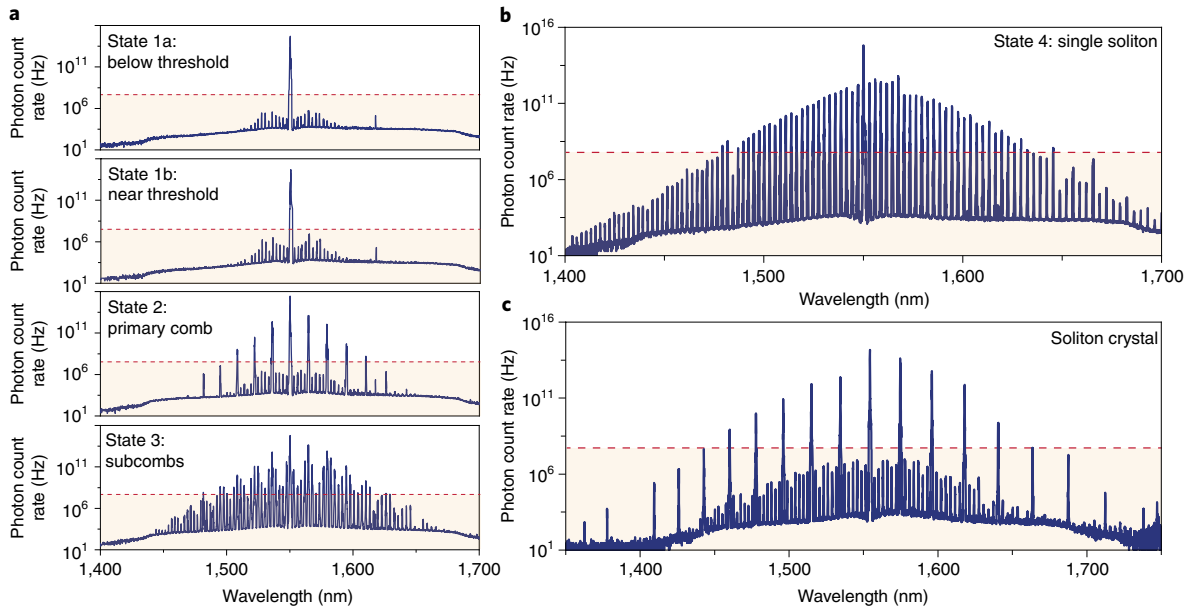

Fig. 2 | Single-photon spectroscopy of optical microcombs. a, The stages of frequency comb formation observed on the SPOSA. The dashed lines indicate the noise floor of a commercial optical spectrum analyser (−80 dBm). **b**, The single soliton state. **c**, A 7-FSR soliton crystal state, observed in a different device.

state and responsible for its quantum-limited timing jitter[29,30] are obscured in the single-soliton spectrum. A perfect soliton crystal[37,38] (henceforth referred to as a soliton crystal), however, reveals these quantum fluctuations (Fig. 2c).

The formation of DKS from a below-threshold quantum frequency comb begins with the transition of a spontaneous FWM process into a stimulated FWM process at the onset of OPO. This transition can be observed through the second-order correlation function, $g^{(2)}(\tau)$. Using input–output theory[41], we derive the exact form of $g^{(2)}(\tau)$ for a general two-mode parametric process. The general derivation is presented in the Supplementary Section 1C. For signal and idler modes of equal linewidths κ, the auto-correlation is given by

$$g^{(2)}_{\mathrm{auto}}(\tau) = 1 + \frac{\mathrm{e}^{-\kappa\tau}}{\lambda^2}\left[\frac{\kappa}{2}\sinh(\lambda\tau) + \lambda\cosh(\lambda\tau)\right]^2 \qquad (2)$$

where $\lambda = \sqrt{g^2 - \delta^2}$ is the effective parametric gain, $g = g_0|A_0|^2$ is the mode coupling strength and δ is the detuning. This bunching in the auto-correlation, with a maximum value of $g^{(2)}_{\mathrm{auto}}(0) = 2$, reflects thermal-state statistics[42]. Two regimes are notable: (1) when $\delta^2 > g^2$, λ is imaginary, which gives rise to oscillations in $g^{(2)}_{\mathrm{auto}}(\tau)$ that

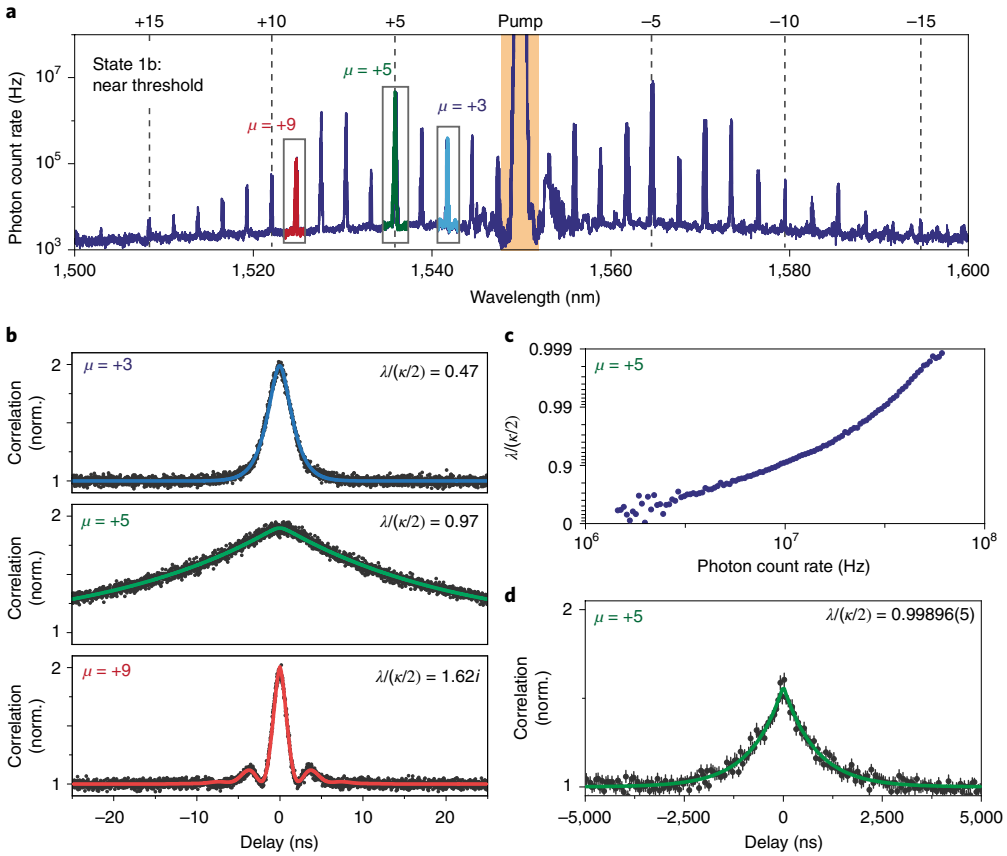

Fig. 3 | Quantum coherence of parametric oscillation. a, The near-threshold spectrum reproduced from Fig. 2a. Vertical dashed lines indicate the modes in which the primary comb will form. **b**, Measured $g^{(2)}_{auto}(\tau)$ on different modes shows the dispersion-dependent parametric gain variation throughout the comb. **c**, Observation of asymptotic growth of coherence near the OPO threshold. The effective parametric gain λ, extracted from a numerical fit to equation (2), is plotted against the detected count rate on mode $\mu = +5$. Here, $\kappa/(2\pi) = 180$ MHz. **d**, At the highest photon count rate, $g^{(2)}_{auto}(\tau)$ reveals coherence-broadening which corresponds to threshold proximity of 0.99896(5). The error bars on the data points represent the standard error.

correspond to the double-peaked photon spectrum for a strongly detuned parametric process[31,36]; and (2) when λ approaches $\kappa/2$, the $g^{(2)}_{auto}(\tau)$ coherence (decay time) increases asymptotically, reflecting the transition of the spontaneous FWM process into a stimulated FWM process (analogous to lasing). Both regimes can be observed simultaneously in a Kerr frequency comb close to but below the OPO threshold (Fig. 3a). We measure $g^{(2)}_{auto}(\tau)$ using two SNSPDs in a Hanbury Brown and Twiss configuration, and observe the dispersion-induced variation in λ for different signal–idler pairs (Fig. 3b)[43]. Mode $\mu = +9$, which is far away from the pump, displays oscillations in $g^{(2)}_{auto}(\tau)$, signifying poor phase-matching. By contrast, mode $\mu = +5$ shows a substantial coherence increase, which correctly predicts that it will seed the formation of the primary comb. To observe the asymptotic coherence growth at threshold, we repeatedly sweep the pump laser detuning through the OPO threshold condition while synchronously acquiring the photon count rates and two-photon correlations. Through the numerical fit to equation (2), λ is extracted and plotted against the measured count rate (Fig. 3c). The maximum recorded coherence broadening exceeds the cavity coherence[41] by nearly three orders of magnitude (Fig. 3d), which indicates that the state is approaching the critical point at which the linearized model would break down[35,36].

In the linearized model of an above-threshold Kerr comb, a resonator mode may be occupied by both a coherent state and quantum fluctuations. In theory, the interference of the coherent state and the quantum fluctuations can be revealed through $g^{(2)}(\tau)$, but the intensity of the former is usually orders of magnitude greater (as can be seen in the spectra of the primary comb and the soliton crystal, Fig. 2), making experimental observation difficult. An exception can be found in the formation of secondary combs. We characterize the quantum formation dynamics of secondary combs through second-order photon correlations (Fig. 4), complementing earlier classical studies[43,44]. By monitoring mode $\mu = +4$, which is equidistant from the pump and the primary sideband, we simultaneously observe the degenerate and non-degenerate spontaneous pair generation processes, as well as the merging of the coherent subcombs. Notably, at the onset of subcombs merging, the intensities of the (bichromatic) coherent state and the quantum optical fields become comparable, and the signature of their interference in two-photon correlations is readily observed (Fig. 4c, state 3a). The Fourier transform (F.T.) of the auto-correlation shows three peaks at 0, $\Delta/2$ and Δ; they represent the two-photon bunching of spontaneous pair generation, the interference of the quantum fluctuations with the bichromatic coherent state, and the radiofrequency beat note[43,44] of the coherent state, respectively. The details of the theory used to model the interference are presented in the Supplementary Section 1E. As the subcombs continue to merge and grow in power (state 3b), the coherent light drowns out the spontaneous parametric processes and the photon correlations correspond to the interference of two weak coherent sources[45].

In a DKS state, the coherent comb is phase-locked and time-independent in the group-velocity reference frame, yielding a time-independent Hamiltonian for the quantum optical fields (equation (1)). By contrast, a comb that is not phase-locked will

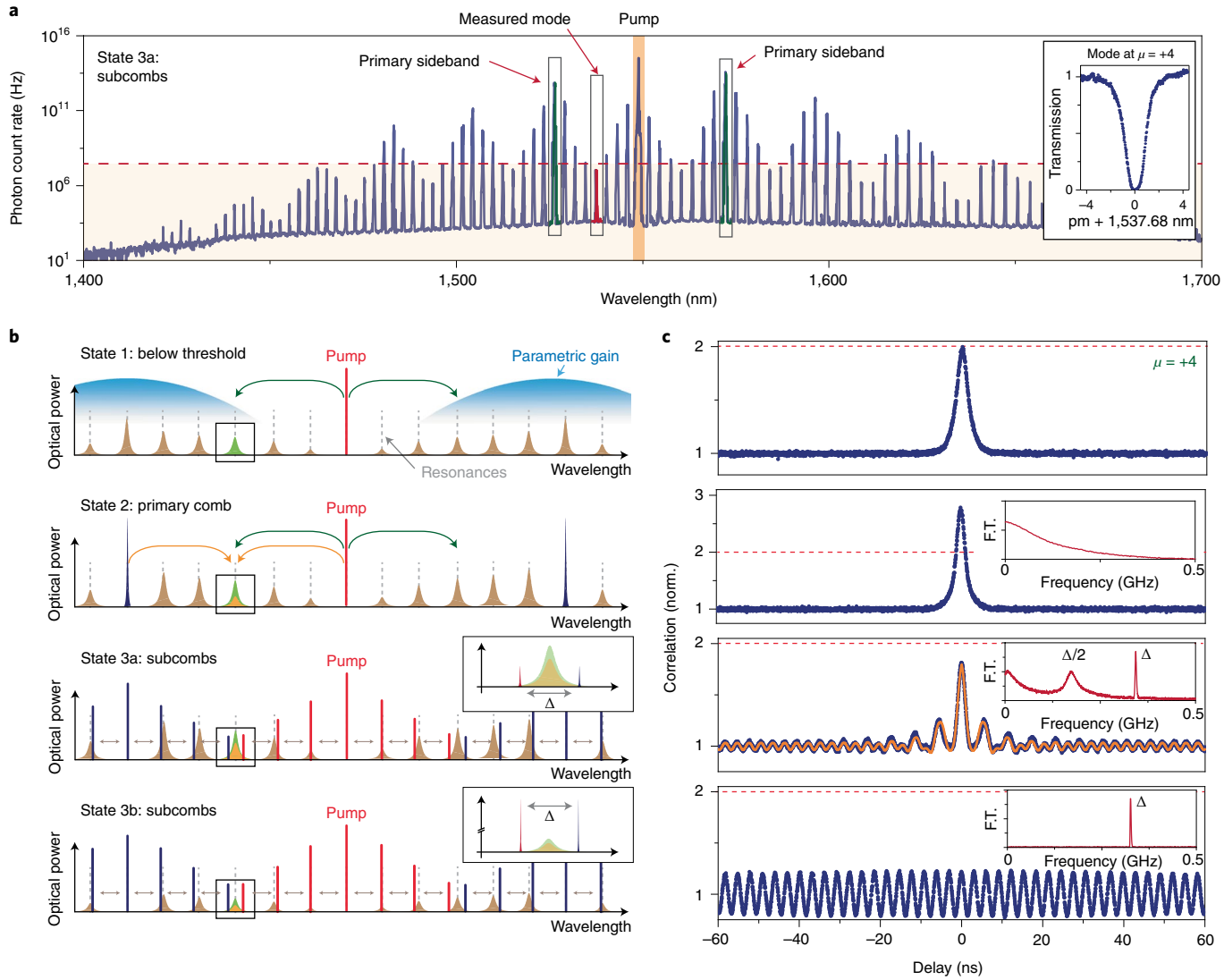

Fig. 4 | Formation dynamics of secondary combs. a, A SPOSA spectrum of a secondary comb state. **b**, A graphical representation of the stages of secondary comb formation. **c**, Auto-correlation is measured at mode $\mu = +4$ for each comb state. In state 1, only non-degenerate pair generation contributes to mode $\mu = +4$. In state 2, simultaneous degenerate and non-degenerate spontaneous pair generation is present. In state 3a, subcombs begin to merge and two-photon correlations reveal the interference of quantum fluctuations with the coherent state. The data are overlaid with the fit to input–output theory. In state 3b, the coherent state dominates and only the radiofrequency beat note is observed.

produce a Hamiltonian with a time-dependent drive. To observe this effect experimentally, we consider a microring resonator that supports three distinct states with 2-FSR spacing: one state is a 2-FSR soliton crystal (Fig. 5a), whereas the others are non-natively spaced secondary combs[43] in the process of merging. These secondary combs are non-phase-locked states, which manifests in the frequency domain as polychromatic comb teeth. For each 2-FSR state, we measure $g^{(2)}(\tau) = \langle g^{(2)}(t,\tau)\rangle_t$ on mode $\mu = -15$ while simultaneously measuring the radiofrequency spectrum of mode $\mu = -6$ on a photodetector. The soliton crystal two-photon correlations are time-independent far from zero time delay. In contrast, the correlations of a non-soliton state exhibit oscillations whose Fourier transform matches the radiofrequency spectrum measured on the photodetector. Such temporal dynamics may be modelled via Floquet theory[46]. We note that similar temporal oscillations in $g^{(2)}(\tau)$ have been observed in Floquet-driven two-level systems[47].

The soliton crystal state offers an excellent opportunity to experimentally verify the linearized model for the DKS state. The mean-field solution (complex amplitudes A_m in equation (1)) of the soliton crystal can be readily computed via the LLE; the below-threshold modes comprise the quantum fluctuations driven by the mean-field solution without any admixture of coherent light and, crucially, they are decoupled from the quantum fluctuations of the above-threshold modes by the mode-matching condition δ_{FWM}. We measure the correlations between all pairs of below-threshold modes of the 2-FSR soliton crystal and compute the theoretically predicted second-order correlations matrix for the measured device parameters (Fig. 5c). We note that the only free parameter in the model is the pump laser detuning (within the soliton locking range). The agreement of the model with the experiment suggests that the quadratic Hamiltonian of the linearized model is indeed appropriate for describing the photon statistics of the quantum optical field generated in the below-threshold modes of a DKS state.

We perform an analysis of the multipartite entanglement across the 2-FSR soliton crystal in the resonator mode basis by computing the logarithmic negativity[48], E_N, for all mode pairs. We find that no pair-wise entanglement is predicted in the measured device in this basis (Fig. 5d). We then consider a modified device architecture,

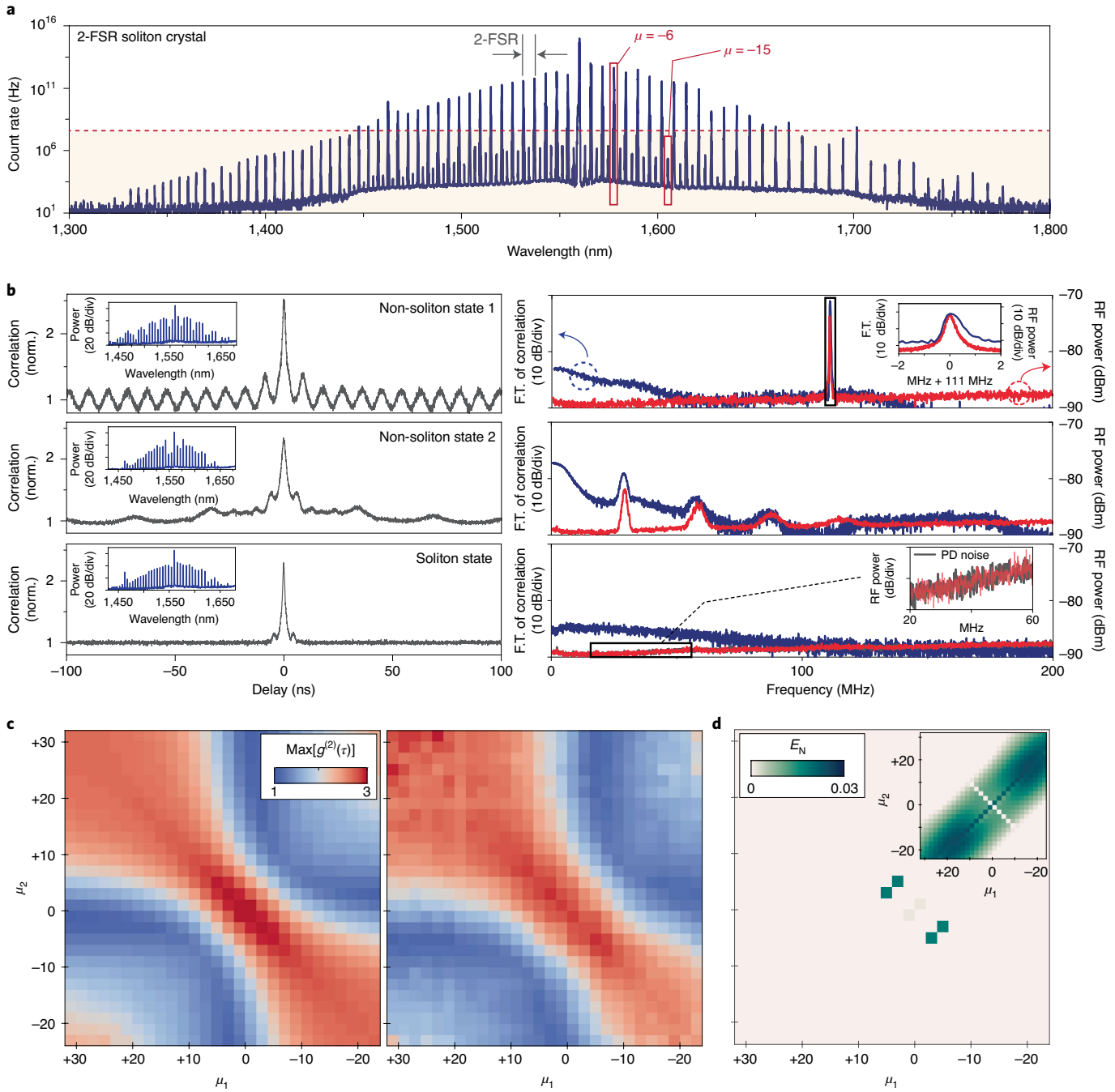

Fig. 5 | Quantum correlations in non-phase-locked combs and perfect soliton crystals. a, A SPOSA spectrum of a 2-FSR soliton crystal. **b**, Left: the measured $g^{(2)}(\tau)$ at mode $\mu = -15$ for different 2-FSR states observed in the device (the inset shows an OSA spectrum of the measured state). Right: the radiofrequency (RF) beat note measured on a photodetector at mode $\mu = -6$ (red) and the Fourier transform of the measured $g^{(2)}(\tau)$ (blue). The bottom panel includes the photodetector (PD) noise floor, corroborating the low-noise soliton state. **c**, The second-order correlations matrix for the below-threshold modes in the 2-FSR soliton crystal. Left: theoretical model. Right: experimental data (60 s acquisition per pixel). **d**, The E_N matrix calculated for the 2-FSR soliton crystal state shows no all-to-all entanglement between the modes. Inset: for a device with tenfold increased out-coupling of the below-threshold modes, all-to-all entanglement is predicted.

where the below-threshold modes are overcoupled to the output waveguide via a photonic molecule configuration (two coupled microresonators)[49,50]. This architecture is advantageous as it allows for the efficient extraction of the quantum optical fields from the device while simultaneously filtering them from the coherent fields, and to independently control the decay rate of the below-threshold modes, all without impacting the soliton crystal (see Supplementary Fig. 6). For this system, we numerically observe all-to-all entanglement along the signal-idler diagonal of the pump. Such an entanglement structure is consistent with the all-to-all connectivity in the 2-FSR soliton crystal Hamiltonian. To gain insight into the strength of multimode entanglement, maximally squeezed supermodes of the soliton crystal must be identified[17]. In ($N > 3$)-FSR soliton crystals, the below threshold modes are not all-to-all coupled. Instead, the modes are divided into disjoint sets grouped by the value $|\mu \bmod N|$, as per the mode-matching condition. Thus,

$\lfloor N/2 \rfloor$ non-interacting subsets (each internally all-to-all coupled) are expected in an N-FSR soliton crystal. Indeed, for the 7-FSR soliton crystal state presented in Fig. 2d, we experimentally confirm three disjoint all-to-all correlated sets of modes (see Supplementary Fig. 7).

In conclusion we have investigated the quantum formation dynamics of DKS states and their quantum correlations. The experimental methods introduced here can serve as a starting point for exploring higher-order corrections to the linearized model both in the DKS and at near-threshold critical points. Applications of DKS states in quantum technologies will be informed by further theoretical and experimental characterization of the intracomb entanglement. Once target supermodes[17] and nullifiers[18,51] are identified for the system, dispersion engineering[52,53] can be employed to design the desired system Hamiltonian. The recent demonstrations of soliton generation in CMOS-foundry photonics[54,55], efficient on-chip frequency translation[56], integrated detection of squeezed light[23], and on-chip squeezed microcombs[24] lay out a clear path toward developing the DKS state as a resource for continuous variable quantum information processing[25–28].

The large-scale multi-mode entanglement possible in a DKS state may also find applications in discrete variable quantum computation protocols operating under continuous wave[5,9] or pulsed[7,8] drive. Although the soliton is traditionally operated in the continuous wave regime, the recent study of solitons driven by a pulsed pump may enable the implementation of time-bin entanglement protocols[57] and the study of the temporal dynamics of quantum correlations[58] under Floquet drive. Pulsed operation can also be achieved with a continuous wave-driven soliton via a time-dependent coupling constant $g_0(t)$ (equation (1)), via the rapidly tunable photonic molecule configuration[49], to realize multimode control of spectral and temporal entanglement in a single integrated photonic device. Finally, we note that with the recent demonstration of Pockels soliton microcombs[59], our results may be further extended to interactions between second- and third-order parametric processes.

Online content

Any methods, additional references, Nature Research reporting summaries, source data, extended data, supplementary information, acknowledgements, peer review information; details of author contributions and competing interests; and statements of data and code availability are available at https://doi.org/10.1038/s41566-021-00901-z.

Received: 18 May 2021; Accepted: 28 September 2021;
Published online: 16 December 2021

References

1. Kippenberg, T. J., Gaeta, A. L., Lipson, M. & Gorodetsky, M. L. Dissipative Kerr solitons in optical microresonators. *Science* **361**, aan8083 (2018).
2. Diddams, S. A., Vahala, K. & Udem, T. Optical frequency combs: coherently uniting the electromagnetic spectrum. *Science* **369**, aay3676 (2020).
3. Kues, M. et al. Quantum optical microcombs. *Nat. Photon.* **13**, 170–179 (2019).
4. Grassani, D. et al. Micrometer-scale integrated silicon source of time-energy entangled photons. *Optica* **2**, 88–94 (2015).
5. Jaramillo-Villegas, J. A. et al. Persistent energy–time entanglement covering multiple resonances of an on-chip biphoton frequency comb. *Optica* **4**, 655–658 (2017).
6. Steiner, T. J. et al. Ultra-bright entangled-photon pair generation from an AlGaAs-on-insulator microring resonator. *PRX Quantum* **2**, 010337 (2021).
7. Reimer, C. et al. Generation of multiphoton entangled quantum states by means of integrated frequency combs. *Science* **351**, 1176–1180 (2016).
8. Kues, M. et al. On-chip generation of high-dimensional entangled quantum states and their coherent control. *Nature* **546**, 622–626 (2017).
9. Samara, F. et al. Entanglement swapping between independent and asynchronous integrated photon-pair sources. *Quantum Sci. Technol.* **6**, 045024 (2021).
10. Vaidya, V. D. et al. Broadband quadrature-squeezed vacuum and nonclassical photon number correlations from a nanophotonic device. *Sci. Adv.* **6**, eaba9186 (2020).
11. Zhao, Y. et al. Near-degenerate quadrature-squeezed vacuum generation on a silicon-nitride chip. *Phys. Rev. Lett.* **124**, 193601 (2020).
12. Arrazola, J. et al. Quantum circuits with many photons on a programmable nanophotonic chip. *Nature* **591**, 54–60 (2021).
13. Suh, M.-G., Yang, Q.-F., Yang, K. Y., Yi, X. & Vahala, K. J. Microresonator soliton dual-comb spectroscopy. *Science* **354**, 600–603 (2016).
14. Riemensberger, J. et al. Massively parallel coherent laser ranging using a soliton microcomb. *Nature* **581**, 164–170 (2020).
15. Spencer, D. T. et al. An optical-frequency synthesizer using integrated photonics. *Nature* **557**, 81–85 (2018).
16. Feldmann, J. et al. Parallel convolutional processing using an integrated photonic tensor core. *Nature* **589**, 52–58 (2021).
17. Roslund, J., De Araujo, R. M., Jiang, S., Fabre, C. & Treps, N. Wavelength-multiplexed quantum networks with ultrafast frequency combs. *Nat. Photon.* **8**, 109–112 (2014).
18. Cai, Y. et al. Multimode entanglement in reconfigurable graph states using optical frequency combs. *Nat. Commun.* **8**, 1–9 (2017).
19. Chen, M., Menicucci, N. C. & Pfister, O. Experimental realization of multipartite entanglement of 60 modes of a quantum optical frequency comb. *Phys. Rev. Lett.* **112**, 120505 (2014).
20. Pfister, O. Continuous-variable quantum computing in the quantum optical frequency comb. *J. Phys. B* **53**, 012001 (2019).
21. Wang, J., Sciarrino, F., Laing, A. & Thompson, M. G. Integrated photonic quantum technologies. *Nat. Photon.* **14**, 273–284 (2020).
22. Wu, B.-H., Alexander, R. N., Liu, S. & Zhang, Z. Quantum computing with multidimensional continuous-variable cluster states in a scalable photonic platform. *Phys. Rev. Res.* **2**, 023138 (2020).
23. Tasker, J. F. et al. Silicon photonics interfaced with integrated electronics for 9 GHz measurement of squeezed light. *Nat. Photon.* **15**, 11–15 (2021).
24. Yang, Z. et al. A squeezed quantum microcomb on a chip. *Nat. Photon.* **12**, 1–8 (2021).
25. Xie, Z. et al. Harnessing high-dimensional hyperentanglement through a biphoton frequency comb. *Nat. Photon.* **9**, 536–542 (2015).
26. Asavanant, W. et al. Generation of time-domain-multiplexed two-dimensional cluster state. *Science* **366**, 373–376 (2019).
27. Larsen, M. V., Guo, X., Breum, C. R., Neergaard-Nielsen, J. S. & Andersen, U. L. Deterministic generation of a two-dimensional cluster state. *Science* **366**, 369–372 (2019).
28. Zhong, H.-S. et al. Quantum computational advantage using photons. *Science* **370**, 1460–1463 (2020).
29. Matsko, A. B. & Maleki, L. On timing jitter of mode locked Kerr frequency combs. *Opt. Express* **21**, 28862–28876 (2013).
30. Bao, C. et al. Quantum diffusion of microcavity solitons. *Nat. Phys.* **17**, 462–466 (2021).
31. Chembo, Y. K. Quantum dynamics of kerr optical frequency combs below and above threshold: spontaneous four-wave mixing, entanglement, and squeezed states of light. *Phys. Rev. A* **93**, 033820 (2016).
32. Chembo, Y. K. & Menyuk, C. R. Spatiotemporal Lugiato–Lefever formalism for Kerr-comb generation in whispering-gallery-mode resonators. *Phys. Rev. A* **87**, 053852 (2013).
33. Haus, H. A. & Lai, Y. Quantum theory of soliton squeezing: a linearized approach. *JOSA B* **7**, 386–392 (1990).
34. Spälter, S., Korolkova, N., König, F., Sizmann, A. & Leuchs, G. Observation of multimode quantum correlations in fiber optical solitons. *Phys. Rev. Lett.* **81**, 786 (1998).
35. Navarrete-Benlloch, C., Roldán, E., Chang, Y. & Shi, T. Regularized linearization for quantum nonlinear optical cavities: application to degenerate optical parametric oscillators. *Opt. Express* **22**, 24010–24023 (2014).
36. Vernon, Z. & Sipe, J. Strongly driven nonlinear quantum optics in microring resonators. *Phys. Rev. A* **92**, 033840 (2015).
37. Cole, D. C., Lamb, E. S., Del'Haye, P., Diddams, S. A. & Papp, S. B. Soliton crystals in Kerr resonators. *Nat. Photon.* **11**, 671–676 (2017).
38. Karpov, M. et al. Dynamics of soliton crystals in optical microresonators. *Nat. Phys.* **15**, 1071–1077 (2019).
39. Guidry, M. A. et al. Optical parametric oscillation in silicon carbide nanophotonics. *Optica* **7**, 1139–1142 (2020).
40. Lukin, D. M. et al. 4H-silicon-carbide-on-insulator for integrated quantum and nonlinear photonics. *Nat. Photon.* **14**, 330–334 (2020).
41. Ou, Z. & Lu, Y. Cavity enhanced spontaneous parametric down-conversion for the prolongation of correlation time between conjugate photons. *Phys. Rev. Lett.* **83**, 2556 (1999).
42. Blauensteiner, B., Herbauts, I., Bettelli, S., Poppe, A. & Hübel, H. Photon bunching in parametric down-conversion with continuous-wave excitation. *Phys. Rev. A* **79**, 063846 (2009).
43. Herr, T. et al. Universal formation dynamics and noise of Kerr-frequency combs in microresonators. *Nat. Photon.* **6**, 480–487 (2012).
44. Coillet, A. et al. On the transition to secondary Kerr combs in whispering-gallery mode resonators. *Opt. Lett.* **44**, 3078–3081 (2019).

45. da Silva, T. F., do Amaral, G. C., Vitoreti, D., Temporão, G. P. & von der Weid, J. P. Spectral characterization of weak coherent state sources based on two-photon interference. *JOSA B* **32**, 545–549 (2015).
46. Navarrete-Benlloch, C., Garcés, R., Mohseni, N. & de Valcárcel, G. Floquet theory for temporal correlations and spectra in time-periodic open quantum systems: application to squeezed parametric oscillation beyond the rotating-wave approximation. *Phys. Rev. A* **103**, 023713 (2021).
47. Lukin, D. M. et al. Spectrally reconfigurable quantum emitters enabled by optimized fast modulation. *npj Quant. Info.* **6**, 1–9 (2020).
48. Vidal, G. & Werner, R. F. Computable measure of entanglement. *Phys. Rev. A* **65**, 032314 (2002).
49. Zhang, M. et al. Electronically programmable photonic molecule. *Nat. Photon.* **13**, 36–40 (2019).
50. Helgason, Ó. B. et al. Dissipative solitons in photonic molecules. *Nat. Photon.* **15**, 305–310 (2021).
51. Ra, Y.-S. et al. Non-gaussian quantum states of a multimode light field. *Nat. Phys.* **16**, 144–147 (2020).
52. Brasch, V. et al. Photonic chip–based optical frequency comb using soliton Cherenkov radiation. *Science* **351**, 357–360 (2016).
53. Lu, X. et al. Chip-integrated visible–telecom entangled photon pair source for quantum communication. *Nat. Phys.* **15**, 373–381 (2019).
54. Jin, W. et al. Hertz-linewidth semiconductor lasers using CMOS-ready ultra-high-Q microresonators. *Nat. Photon.* **15**, 346–353 (2021).
55. Xiang, C. et al. Laser soliton microcombs heterogeneously integrated on silicon. *Science* **373**, 99–103 (2021).
56. Hu, Y. et al. On-chip electro-optic frequency shifters and beam splitters. *Nature* **599**, 587–593 (2021).
57. Daugey, T., Billet, C., Dudley, J., Merolla, J.-M. & Chembo, Y. K. Kerr optical frequency comb generation using whispering-gallery-mode resonators in the pulsed-pump regime. *Phys. Rev. A* **103**, 023521 (2021).
58. Imany, P., Lingaraju, N. B., Alshaykh, M. S., Leaird, D. E. & Weiner, A. M. Probing quantum walks through coherent control of high-dimensionally entangled photons. *Sci. Adv.* **6**, eaba8066 (2020).
59. Bruch, A. W. et al. Pockels soliton microcomb. *Nat. Photon.* **15**, 21–27 (2021).

Methods

Experimental set-up. Thin films of monocrystalline 4H-SiC are used[40] to fabricate the SiC resonators used in this work. Bulk, high-purity semi-insulating SiC crystals were purchased from Cree Inc. The devices are patterned via e-beam lithography using ZEP52A e-beam resist (Zeon Corp) combined with an aluminium hard-mask to increase the SiC etching selectivity[39]. Broadband inverse-designed vertical couplers are used to couple light to and from the device[39]. The device is operated at 4 K to reduce the thermo-optic response[60]. In the design of the SPOSA, we focused on broadband operation to image all parts of the frequency comb, which extends beyond the operation range of standard fibre-based filtering components. For this reason, a free-space monochromator approach was chosen. Blazed gratings (600 grooves per millimetre) optimized for 1.5 µm operated in the Littrow configuration have 75–85% efficiency across the range of operation (1,300–1,700 nm). The bandwidth is further limited by chromatic aberration of free-space focusing optics, causing a total efficiency roll-off below 20% outside of the 200 nm range around the centre wavelength of 1,550 nm. In a single-pass monochromator, dynamic range is limited to around 70 dB by roughness-induced scattering from the grating surface. By operating the monochromator in a two-pass configuration, where the forward and return beams do not overlap on the grating, the dynamic range is doubled. A second, single-pass monochromator can also be used to further increase the dynamic range. The double-pass monochromator configuration has dynamic range in excess of 180 dB and total peak efficiency as high as 55%. The SNSPDs are optimized for broadband operation with efficiency exceeding 80% from 1.0–1.6 µm, while maintaining a low dark count rate of 5 Hz. The experimental set-up is presented in Supplementary Fig. 2. We note that although the SPOSA was essential for this study, it may be possible to combine existing technologies—such as fibre filters[7], programmable pulse-shapers[5,8] and on-chip filtering—to achieve similar functionality.

Modelling of two-photon correlations. Two-photon correlations are computed analytically and/or numerically via the input–output formalism. The two-photon correlations are normalized to the total count rate and thus do not depend upon the absolute photon collection efficiency. Details of the derivation are presented in the Supplementary Section 1. The mean-field solution used as the driving term in the computation is obtained via LLE simulation. Supplementary Fig. 1 illustrates the combination of LLE and input–output formalism in the near-threshold case.

Data availability

The data that support the findings of this study are available from the corresponding author on request.

Code availability

The code used in this study is available from the corresponding author on request.

References

60. Moille, G. et al. Kerr-microresonator soliton frequency combs at cryogenic temperatures. *Phys. Rev. Appl.* **12**, 034057 (2019).

Acknowledgements

We gratefully acknowledge discussions with J. Bowers, T. Zhong, L. Chang, C. Bao, B. Shen, A. Dutt and S. Sun. This work is funded by the Defense Advanced Research Projects Agency under the PIPES and LUMOS programmes and by the IET AF Harvey Prize. M.A.G. acknowledges the Albion Hewlett Stanford Graduate Fellowship (SGF) and the NSF Graduate Research Fellowship. D.M.L. acknowledges the Fong SGF and the National Defense Science and Engineering Graduate Fellowship. Part of this work was performed at the Stanford Nanofabrication Facility (SNF) and the Stanford Nano Shared Facilities (SNSF).

Author contributions

M.A.G., D.M.L., K.Y.Y. and J.V. conceived the experiment. M.A.G. conducted quantum correlations theory. K.Y.Y, M.A.G. and D.M.L. conducted soliton generation experiments. D.M.L, M.A.G. and K.Y.Y. conducted quantum correlations experiments. D.M.L. fabricated the devices. D.M.L., K.Y.Y. and M.A.G. conducted LLE simulations. M.A.G. and R.T. performed the entanglement calculation. R.T. provided theoretical guidance. J.V. supervised the project. All authors discussed the results and contributed to the final manuscript.

Competing interests

The authors declare no competing interests.

Additional information

Supplementary information The online version contains supplementary material available at https://doi.org/10.1038/s41566-021-00901-z.

Correspondence and requests for materials should be addressed to Jelena Vučković.

Peer review information *Nature Photonics* thanks the anonymous reviewers for their contribution to the peer review of this work.

Reprints and permissions information is available at www.nature.com/reprints.